



HHS Public Access

Author manuscript

Small. Author manuscript; available in PMC 2023 March 08.

Published in final edited form as:

Small. 2022 September ; 18(36): e2202309. doi:10.1002/sml.202202309.

Biostimulatory Micro-fragmented Nanofiber-Hydrogel Composite Improves Mesenchymal Stem Cell Delivery and Soft Tissue Remodelling

Zhi-Cheng Yao,

Department of Materials Science and Engineering, Johns Hopkins University, Baltimore, MD 21218, USA

Translational Tissue Engineering Center, Johns Hopkins University School of Medicine, Baltimore, MD 21213, USA

Institute for NanoBioTechnology, Johns Hopkins University, Baltimore, MD 21218, USA

Dr. Yueh-Hsun Yang,

Translational Tissue Engineering Center, Johns Hopkins University School of Medicine, Baltimore, MD 21213, USA

Department of Plastic and Reconstructive Surgery, Johns Hopkins School of Medicine, Baltimore, MD 21287, USA

Jiayuan Kong,

Department of Materials Science and Engineering, Johns Hopkins University, Baltimore, MD 21218, USA

Translational Tissue Engineering Center, Johns Hopkins University School of Medicine, Baltimore, MD 21213, USA

Institute for NanoBioTechnology, Johns Hopkins University, Baltimore, MD 21218, USA

Yining Zhu,

Translational Tissue Engineering Center, Johns Hopkins University School of Medicine, Baltimore, MD 21213, USA

Institute for NanoBioTechnology, Johns Hopkins University, Baltimore, MD 21218, USA

Department of Biomedical Engineering, Johns Hopkins University School of Medicine, Baltimore, MD 21205, USA

Dr. Ling Li,

hmao@jhu.edu (H.-Q. M.).

Supporting Information

Supporting Information is available from the Wiley Online Library or from the author.

Conflict of Interest

HQM and SKR are co-founders of LifeSprout Inc., a start-up company that has licensed the technology described in this manuscript. Under a licensing agreement between LifeSprout Inc. and the Johns Hopkins University, HQM and SKR are entitled to shares of royalty received by the University on sales of products described in this article. HQM, SKR, and the University own LifeSprout Inc. stock, which is subject to certain restrictions under the University policy. HQM and SKR are also paid consultants to LifeSprout Inc. This arrangement has been reviewed and approved by the Johns Hopkins University in accordance with its conflict-of-interest policies.

Division of Gastroenterology and Hepatology, Johns Hopkins University School of Medicine, Baltimore, MD 21287, USA

Dr. Calvin Chang,

Translational Tissue Engineering Center, Johns Hopkins University School of Medicine, Baltimore, MD 21213, USA

Institute for NanoBioTechnology, Johns Hopkins University, Baltimore, MD 21218, USA

Department of Biomedical Engineering, Johns Hopkins University School of Medicine, Baltimore, MD 21205, USA

Dr. Chi Zhang,

Department of Materials Science and Engineering, Johns Hopkins University, Baltimore, MD 21218, USA

Translational Tissue Engineering Center, Johns Hopkins University School of Medicine, Baltimore, MD 21213, USA

Institute for NanoBioTechnology, Johns Hopkins University, Baltimore, MD 21218, USA

Jason Yin,

Department of Materials Science and Engineering, Johns Hopkins University, Baltimore, MD 21218, USA

Translational Tissue Engineering Center, Johns Hopkins University School of Medicine, Baltimore, MD 21213, USA

Institute for NanoBioTechnology, Johns Hopkins University, Baltimore, MD 21218, USA

Jeffrey Chao,

Translational Tissue Engineering Center, Johns Hopkins University School of Medicine, Baltimore, MD 21213, USA

Institute for NanoBioTechnology, Johns Hopkins University, Baltimore, MD 21218, USA

Department of Public Health Studies, Krieger School of Arts and Sciences, Johns Hopkins University, Baltimore, MD 21218, USA

Prof. Florin M. Selaru,

Division of Gastroenterology and Hepatology, Johns Hopkins University School of Medicine, Baltimore, MD 21287, USA

Prof. Sashank K. Reddy,

Institute for NanoBioTechnology, Johns Hopkins University, Baltimore, MD 21218, USA

Department of Plastic and Reconstructive Surgery, Johns Hopkins School of Medicine, Baltimore, MD 21287, USA

Department of Biomedical Engineering, Johns Hopkins University School of Medicine, Baltimore, MD 21205, USA

Prof. Hai-Quan Mao

Department of Materials Science and Engineering, Johns Hopkins University, Baltimore, MD 21218, USA

Translational Tissue Engineering Center, Johns Hopkins University School of Medicine, Baltimore, MD 21213, USA

Institute for NanoBioTechnology, Johns Hopkins University, Baltimore, MD 21218, USA

Department of Biomedical Engineering, Johns Hopkins University School of Medicine, Baltimore, MD 21205, USA

Abstract

Functional microgels are preferred stem cell carriers due to the ease of delivery through minimally invasive injection and seamless integration with the surrounding host tissue. We have previously developed a biostimulatory nanofiber-hydrogel composite (NHC) through covalently crosslinking a hyaluronic acid hydrogel network with surface-functionalized poly (ϵ -caprolactone) nanofibre fragments. The NHC mimics the microarchitecture of native soft tissue matrix, showing enhanced cell infiltration, immunomodulation, and proangiogenic properties. Here, we improved injectability of the pre-formed NHC by mechanical fragmentation, making it into micro-fragmented NHC (mfNHC) in a granular gel form as a stem cell carrier to deliver mesenchymal stem cells (MSCs) for soft tissue remodelling. The mfNHC showed similar storage modulus but a significantly reduced injection force, as compared with the corresponding bulk NHC. When injected subcutaneously in a rat model, mfNHC-MSC constructs initiated an elevated level of host macrophage infiltration, more pro-regenerative polarization and subsequently, improved angiogenesis and adipogenesis response when compared to mfNHC alone. A similar trend of host cell infiltration and pro-angiogenic response was detected in a swine model with a larger volume injection. These results suggest a strong potential for use of the mfNHC as an injectable carrier for cell delivery and soft tissue remodelling.

Keywords

nanofibre-hydrogel composite; granular hydrogel; stem cell delivery; macrophage; soft tissue remodelling

1. Introduction

Soft tissue defect remains a significant obstacle in reconstructive surgery, ranging from mild cases, such as contour incongruencies caused by congenital deformities to large volume tissue loss following deep burns, trauma or tumour resection.^[1] A fundamental challenge for soft tissue regeneration is the reconstruction of microvascular networks in the ischemia area, which provides oxygen and nutrition to support cell growth and metabolism.^[2] Angiogenesis is the primary process of new vessel formation in soft tissue regeneration, beginning with new vessels sprouting from adjacent intact blood vessels and further growing into the implant.^[3] To facilitate soft tissue remodelling, mesenchymal stem cells (MSCs) have been used to provide bioactive cues to promote macrophage polarization toward an anti-inflammatory/immune regulatory phenotype during the process.^[4, 5] However, direct stem cell transplantation usually results in poor cell retention at the tissue repair site when injected directly into the harsh microenvironment, leading to immune attack and rapid apoptosis of the implanted cells due to the innate and adaptive immune responses.^[6-9]

A wide range of scaffolds and functional matrices have been used as carriers to enhance cell delivery and retention of MSCs.^[9–11] Among them, hydrogels remain the most commonly-used matrices for cell delivery, cell retention support and tissue regeneration because of their similarities in mechanical properties and hydrated microenvironment to the native soft tissues.^[12, 13] Hyaluronic acid (HA) hydrogel is the most widely used due to its excellent biocompatibility, biodegradability, and ease of functionalization.^[14, 15] One common limitation of the hydrogel matrix is its limited ability to permit host cell infiltration when the stiffness of the hydrogel reaches a sufficiently high level matching that of soft tissue, in order to maintain repair site integrity and resist surrounding tissue pressure. As a result, the pore size of the hydrogel is relatively low, limiting cell migration. To address this issue, we previously developed a nanofiber-hydrogel composite (NHC) consisting of a HA hydrogel network covalently linked to electrospun poly(ϵ -caprolactone) (PCL) nanofiber fragments forming an integrated composite structure.^[16, 17] In contrast to a physical blend of HA hydrogel and PCL fibre fragments, the interfacial bonding between the nanofibers and the hydrogel network provides substantial mechanical reinforcement while permitting sufficiently large pore sizes (tens of microns) and porosity (more than 95%) for cell migration in the matrix and host cell recruitment.^[16] More importantly, the larger pore size of the NHC is critical for its immunomodulatory property, which enhances angiogenic response and blood vessel ingrowth into the NHC. This unique property together with its ability to retain its shape and uphold the mechanical integrity at the injection site, makes it an excellent stem cell delivery matrix for tissue regeneration and repair.

A typical method using NHC for cell delivery is to mix the hydrogel precursor solutions right before injection and following *in-vivo* delivery, a bulk composite forms gradually as a result of *in-situ* crosslinking to achieve the desired stiffness.^[16, 17] Most bulk hydrogels rely on a homogeneous precursor solution to exhibit low viscosity until gelation can be induced through *in-situ* crosslinking approaches for injectability. However, gelation time may alter the performance of the hydrogel *in vivo* depending on the preparation and gelation kinetics. A pre-formed NHC can remove the variability due to the gelation kinetics and sample preparation factors; however, it is more difficult to implant the bulk matrix, which needs to be shaped first and implanted together with cells through surgical incisions.

Hydrogel microparticles or microgels can be pre-formed and are easily injectable with an appropriately sized needle. In addition, the cells in un-crosslinked hydrogel precursor are subject to significant shear force during the injection process, and crosslinking chemistry is also limited to those that can occur at body temperature and ambient conditions.^[18] At the individual particle level, microgels are not only able to retain the structural and functional features of the bulk gel, but also anneal to volumize after being injected into a confined tissue space. Microgel size range and heterogeneity can influence the packing density, the void space between particles, and the overall porosity depending on the injection site.^[19, 20] More importantly, microgels can be considered an off-the-shelf product and can be mixed with cells before injection. Similar to the *in-situ* formed hydrogel, microgels can also fill irregular shaped defects after injection.^[21] There are a variety of microgel fabrication techniques including microemulsion, microfluidic droplets, lithography, electrohydrodynamic spraying, and mechanical fragmentation.^[22–24] Here, we developed a method to generate microgels from NHC *via* mechanical fragmentation (Figure 1A).

This method offers distinct advantages of improved scalability and less dependency on gelation time and precursor viscosity seen in alternative approaches. The pre-formed NHC is physically modulated, by being pushed through a mesh screen, installed between two connected syringes, creating a population of aspherical micro-fragmented NHC in a granular gel form. This screening system allows for good control over the size of the granular beads, thus modulating the size as needed. In some embodiments, different mesh size sieves used to process the bulk composite can yield to different histograms for the bead size. The bead size was varied by varying the mesh size of the screens used in the beading process.

In this study, we compared the mechanical properties and injectability of these mechanical-fragmented NHC (mfNHC) with the bulk NHC counterpart and demonstrated their advantages for cell delivery in rat and swine models using allogeneic bone marrow-derived MSCs (Figure 1A). Using these models, the effect of mfNHC delivery on MSC retention, host cellular infiltration, macrophage polarization, and pro-angiogenesis responses were assessed.

2. Results and Discussion

2.1. Synthesis of mfNHC

Here we developed a new crosslinking scheme over our previous reports in an effort to simplify the synthesis process for HA hydrogel.^[16, 17] We first prepared the NHC precursor HA-Ac by reacting glycidyl acrylate with HA and forming acrylate groups conjugated to the backbone of HA. The ¹H-NMR spectrum of HA-Ac (Figure S1) showed characteristic peaks of glycidyl acrylate units were observed at 5.85–6.40 ppm, assigned to vinyl protons (O=C–(CH=CH₂)) in acrylate groups.^[26, 27] The acrylation degree of HA-Ac prepared under this condition was estimated to be 9.8 ± 0.3 % in reference to the number of repeating units in HA. In parallel, electrospun PCL nanofibers prepared using a previously reported method were treated with plasma activation to generate carboxylic groups on the fibre surface. The average density of the carboxylic groups was controlled to be 125 ± 25 nmol/mg using a toluidine blue O assay following the method in our previous study.^[16] Next, the carboxyl groups were converted to the thiol-reactive MAL group by reacting the carboxylic fibres with a large excess of AE-MAL to generate MAL-functionalized PCL (MAL-PCL) nanofibers. After washing, the functionalized PCL fiber fragments were cryo-milled to generate fibre fragments with a length ranging from 40 to 80 μm , and an average of 56.1 ± 11.3 μm . The NHC was then synthesized by crosslinking MAL-PCL fibre fragments, HA-Ac and PEG-SH at the final concentrations of 30 mg mL^{-1} , 10 mg mL^{-1} , and 5 mg mL^{-1} , respectively, at 37°C for complete gelation forming an integrated composite structure (Figure 1B). As we have shown previously using a different crosslinking scheme,^[16] the mechanical property and the average pore size of the NHC depend on the network crosslinking density, which influences the permeability of macromolecules and migration of cells.^[28, 29] We selected the concentrations and modification degrees of the various components (HA-Ac, MAL-PCL, PEG-SH) and this synthesis protocol to obtain a NHC with a targeted shear storage modulus G' of $213.6 \pm 21.9 \text{ Pa}$ and loss modulus G'' of $17.3 \pm 2.8 \text{ Pa}$.

To produce mfNHC with different sizes from the NHC, we used a mechanical fragmentation method by passing the pre-formed NHC bulk gel through a stainless-steel mesh screen with well-defined pore sizes.^[30] Three mesh screens with opening pore sizes of 0.003, 0.006, and 0.009 inches were used in this study to prepare mfNHC with 3 different particle sizes. As the pore size of the mesh screen increased from 0.003, 0.006, and 0.009 inches, the average particle size of the mfNHC also increased from $131.3 \pm 18.8 \mu\text{m}$ to $213.4 \pm 49.6 \mu\text{m}$ and $391.6 \pm 104.8 \mu\text{m}$ correspondingly (Figure 1C, fluorescently labelled mfNHC were shown in Figure S2). Compared to the bulk NHC gel, the injection force of the mfNHC was significantly reduced from $35.4 \pm 1.0 \text{ N}$ (bulk NHC) to $11.6 \pm 0.9 \text{ N}$ (131- μm mfNHC) (Figure 1D). As expected, the injection force of the mfNHC increased with increasing the particle size, measuring $11.6 \pm 0.9 \text{ N}$, $27.5 \pm 2.3 \text{ N}$, and $31.7 \pm 1.3 \text{ N}$ for the 131- μm , 213- μm , and 392- μm mfNHC, respectively. Additionally, the rheological assessments indicated that the beading process did not significantly change the measured storage modulus G' of the NHC, which remained at $204.8 \pm 14.4 \text{ Pa}$ to $216.5 \pm 23.9 \text{ Pa}$ range for all NHC bulk and mfNHC (Figure 1E).

The mechanical fragmentation method adopted in this manuscript is advantageous due to its simplicity and scalability. Most of other microgel fabrication methods are limited to faster gelation process. For a slow forming hydrogel or our NHC, mechanical fragmentation is most appropriate as it is independent of the gelation time or precursor viscosity. Passing a pre-formed NHC through a stainless-steel mesh with defined pore size generates mfNHC beads. The mfNHC generated with this simple method consists of microgels with aspherical shape and a relatively narrow size distribution. The average size of the mfNHC can be controlled by the mesh size of the screen used in the mechanical fragmentation process. This method can be easily converted to a continuous beading process for a scaled-up manufacture. These results indicated that the irregular shaped mfNHC had an ability to re-anneal, retaining mechanical properties, under compression (such as following s.c. injection) or mechanical shear conditions (such as under the rheology testing condition). The mechanical fragmentation process shown here significantly improved injectability of the NHC gel without influencing its rheological properties. For the rest of this study, we use the mfNHC with an average size of $131 \mu\text{m}$ to assess its performance for MSC delivery.

2.2. mfNHC as a carrier to deliver MSCs

We tested the cell retention ability of the mfNHC in a rat model following s.c. injection. For the bulk gel delivery group, one million MSCs were mixed with NHC gel precursor mixture at 30 min after mixing all the active components (HA-Ac, MAL-PCL fibers, and PEG-SH) using a syringe union and mixing cells and the gelling suspension by back-and-forth extrusions in two 1-cc syringes and injected the mixture within 30 min after mixing. For the mfNHC group, the NHC beads were mixed with MSC suspension using the same syringe extrusion method and injected immediately after mixing. As indicated in Figure 1F, on day 3, MSCs delivered in mfNHC and *in situ* formed NHC gel showed similar cell retention rates as $94.2 \pm 8.9\%$ and $88.4 \pm 3.9\%$, respectively, comparable to direct MSC injection (cell retention rate, $82.2 \pm 11.0\%$). On day 7, MSC retention rates for the mfNHC and the *in-situ* gel groups were $84.3 \pm 12.4\%$ and $82.1 \pm 16.1\%$, respectively, whereas the MSC injection group has lost nearly all the injected cells starting from POD 7 (retention

rate, $0.7 \pm 0.1\%$, Figure 1G). There was no significant difference between the mfNHC and *in-situ* NHC groups throughout the 14-day period experiment, confirming that these irregularly shaped mfNHC were able to anneal and reform a gel matrix similar to the *in-situ* formed NHC gel. This result revealed the mfNHC prolonged MSC retention *in-vivo* proving the potential of the mfNHC as an effective MSC carrier for tissue regenerative application.

2.3. Shape retention of the subcutaneously injected mfNHC with or without MSCs

MRI with volumetric analysis as an effective, accurate, safe and non-invasive translational approach to evaluate the biodegradability of hydrogel materials, providing a unique signature to visualize the implant, was used in this study to assess the mfNHC shape retention in rats following s.c. injection.^[31] Using this method, we were able to serially monitor the shape and volume of the injected matrix and/or MSCs over time. As shown in Figure 2A, the injected volume of the MSC suspension was quickly lost, as we anticipated from the cell retention experiment (Figure. 1F). There was slight swelling for both mfNHC and mfNHC-MSc co-injection on POD 7 and then gradual decreases in the total volume for both groups. By POD 28, the volume retention of the mfNHC-MSc decreased to $59.1 \pm 7.4\%$, compared to $89.0 \pm 18.5\%$ of the mfNHC alone (Figure 2B). Nonetheless, the difference in trends between these two groups were not statistically significant, indicating that the delivering MSCs with mfNHC at this tested condition did not significantly influence the shape retention of the mfNHC.

2.4. Host cell infiltration and macrophage polarization inside the subcutaneously injected mfNHC with or without MSCs

Cell infiltration fronts inside the NHC matrix over 28 days were visualized by H&E staining (Figure 2C). A significantly increased cell infiltration degree was observed within the injected mfNHC when MSCs were co-injected (a thicker boundary pointed by arrows in Figure 2C). At the earlier time points (PODs 3 and 14), the proportion of cell infiltrated area in the mfNHC encapsulating MSCs was approximately twice when compared to mfNHC without MSCs: $50.1 \pm 7.0\%$ vs. $22.2 \pm 8.8\%$ on POD 3 and increased to $62.1 \pm 0.9\%$ vs. $35.2 \pm 9.3\%$ on POD 14. On POD 28, the proportion of cell infiltrated area for mfNHC increased to $56.6 \pm 5.6\%$, which was closer to that for mfNHC-MSc co-injection ($72.7 \pm 12.9\%$); there was no significant difference between these two groups on POD 28.

At POD 21, FACS analysis was conducted to quantify the proportion of DiR-labeled MSCs among the total cells recovered from the injected matrix. Both the mfNHC and *in-situ* formed NHC showed similar percentages of DiR⁺ MSCs (about 20% of the recovered cells found inside the matrix), whereas no DiR⁺ MSCs were detected in the tissue around the MSC injection site for the MSC group (Figure 3A).

To evaluate the infiltration of monocyte and macrophage phenotypes within the injected mfNHC with or without MSCs at different time points after injection, the matrix was retrieved and the percentages of monocytes (CD68⁺), M1-like macrophages (CD68⁺CD38⁺), and M2-like macrophages (CD68⁺CD163⁺) were examined by FACS.^[32-34] At POD 7, there was no significant difference in the total macrophage infiltration degree between the mfNHC injected with ($23.4 \pm 2.4\%$) and without MSCs ($21.6 \pm 3.6\%$). At POD 21,

compared to the mfNHC group, a markedly increased infiltration of monocytes (nearly 2-fold elevation) was observed for the MSC encapsulated mfNHC: $65.5 \pm 2.4\%$ for mfNHC-MS group vs. $37.3 \pm 3.0\%$ for mfNHC group (Figure 3B). In addition, it was found that at POD 21, a significantly higher percentage ($42.0 \pm 3.1\%$) of M2-like macrophages were found in the mfNHC-MS group than that ($30.4 \pm 3.0\%$) in the mfNHC group, while there was no significant difference in the percentage of M1-like macrophages between the two groups (Figure 3D). As shown in Figure 3C, the immunofluorescent staining at POD 3 and POD 28 also indicates that the mfNHC-MS group induced a pro-regenerative effect *in vivo* (tile-scanned images were shown in Figure S3).

The results above indicate that by incorporating MSCs, the infiltration level of M2-like macrophages ($CD68^+CD163^+$) within the composite is further elevated, which plays a critical role during the tissue regeneration process. This study primarily focuses on the monocytes and macrophages due to the early arrival of these cells and their role in immune conditioning of the local microenvironment during the early phase of the remodelling process. Monocytes/macrophages play a vital role in eliciting the initial pro-inflammatory response and orchestrating the pro-regenerative process.^[35, 36] Macrophage polarization toward different phenotypes, including pro-inflammatory (M1 like) and pro-regenerative (M2 like) polarization initiates the later stage immune response in the matrix.^[37, 38] The roles of other immune cells, particularly T cells, will be investigated in future studies.

2.5. Enhanced angiogenesis and adipogenesis in MSC-encapsulated mfNHC following subcutaneous injection

The collected tissue sections were stained with Masson's trichrome to reveal matrix remodelling and collagen deposition within the injected matrix (Figure S4) over 28 days. Evenly distributed collagen was detected inside the mfNHC-MS construct. Immunofluorescent staining was used to examine tissue sections harvested from the mfNHC-MS and mfNHC groups at POD 14 and 28. The staining results (Figure 4A) showed the presence of infiltrated RECA-1⁺ endothelial cells in the matrix. In addition, endothelial cell-associated pericytes were also stained with α -smooth muscle actin (α -SMA) antibody to assist with the identification (Figure. S5). Since the analysis was monitored for only 4 weeks after implantation, most of the newly formed blood vessels were still structurally immature such that the smooth muscle layer and endothelium did not always align perfectly; and some endothelial cells were observed in the vessel lumen, as expected in the neovascular capillaries. The co-occurrence of RECA-1⁺ endothelial cells surrounded by α SMA⁺ pericytes was counted to quantify the endothelial cell density in cell-infiltrated areas, which increased over time (Figure 4B). More importantly, the endothelial cell density in the cell infiltrated area was enhanced by co-delivering allogenic MSCs with the mfNHC as compared with mfNHC injection alone at POD 28. To further explore the soft tissue remodelling process inside the matrix, tissue sections from PODs 14 and 28 were stained with Perilipin-1 and Acrp-30 to assess the promotion of adipogenesis. In Figure 4C, it was found that the implanted MSCs helped stimulate adiponectin and adipocyte formation inside the injected matrix near the boundary starting from POD 14 and continuing until POD 28.

It has been reported that MSCs provide immunomodulation and paracrine effects in a tissue repair and remodelling site.^[39, 40] To evaluate the effect of MSCs in promoting host tissue ingrowth, a rat cytokine antibody proteome profiler array was used to assess the inflammation- and regeneration-related cytokines and chemokines. To eliminate individual difference, the normal tissue control and the NHC matrix were dissected on day 14 and day 28 after the subcutaneous injection. In Figure S6, the results showed changes induced by MSCs in multiple cytokine regulation such as VEGF, DPPIV, HGF, ICAM-1, MMP-2, which have been widely recognized as effective and specific growth factors that can promote tissue regeneration,^[41, 42] were significantly upregulated in the mfNHC-MSc group.

In addition, Figure 4D presents two categories of cytokines and chemokines related to immunomodulation and tissue remodelling from the full panel of the array. With increasing time post-implantation, the initial immunomodulation response (CCL3, CCL5, CXCL2, GDF-15, GM-CSF, IL-1 β , IL-17A) was elevated in both the mfNHC and mfNHC-MSc groups, while the mfNHC-MSc showed a significantly higher level over mfNHC only. This result is consistent with the flow cytometry data in Figure 3A. These results indicated that soft tissue remodelling process increased with time, and the mfNHC-MSc co-injection presented a more pronounced remodelling response (Acrp30, DPPIV, EGF, FGF-7, ICAM-1, MMP-2, VEGF) compared to the mfNHC group.

2.6. Host cell infiltration and tissue remodelling mediated by mfNHC with or without MSCs in a swine model

Larger defects may require a larger amount of mfNHC which could pose limitations in terms of cell migration. To this end, we utilized swine as a large animal model that allows testing for larger amounts of mfNHC. To assess the angiogenesis potential of this mfNHC-MSc construct in a large animal model, we tested this approach in a swine model following subcutaneous injection of 500 μ L of mfNHC with and without 2.5 million allogeneic adipose-derived MSCs isolated from fat tissue harvested from other pigs in the same cohort. Volume retention and host cell infiltration inside the injected constructs were characterized at PODs 14 and 56. H&E staining of the tissue sections of the collected injection site (Figure 5A) indicated that host cells infiltrated the matrix faster than that observed in rats; the entire matrix was infiltrated by host cells by 2 weeks in both the mfNHC and mfNHC-MSc constructs. There were more adipocytes observed inside the mfNHC-MSc construct than that in mfNHC only at POD 14. However, no distinctive variance of the implants was detected over the 56-day period. Using callipers to estimate the retention volume variation of the injectant over the 56-day period, the volumes of the constructs were similar, $396.2 \pm 31.6 \mu$ L and $390.1 \pm 28.0 \mu$ L for the mfNHC-MSc and mfNHC groups, respectively, indicating strong volume retention in both groups (Figure 5B). To further explore the pro-angiogenesis effect inside the constructs, endothelial cells were marked by α SMA *via* immunofluorescent staining. Confocal images in Figure 5C show that endothelial cell density inside the mfNHC-MSc construct (68.2 ± 11.4 per mm^2) was markedly higher than that in the mfNHC group (33.5 ± 12.0 per mm^2) at POD 14 (Figure 5D).

3. Conclusion

We developed a novel injectable mfNHC comprised of a nanofiber-hydrogel composite as a carrier for MSCs delivery to promote cell retention and tissue remodelling. The mfNHC microparticles were generated by mechanical fragmentation method with a reasonable level of control over particle size based on dimensions of a mesh screen. The mfNHC showed improved injectability while maintaining the same shear storage modulus. Used as MSC carrier for subcutaneous injection in SD rats, the mfNHC worked as well as the *in-situ* crosslinked NHC in MSC retention. The MSC-encapsulated mfNHC delivered by mfNHC-MS-C co-injection showed a higher rate of host monocyte and macrophage infiltration, greater polarization towards the pro-regenerative phenotype and facilitation of angiogenesis. These results indicated that transplanted mfMSCs augmented immunomodulation and the tissue remodelling process over mfNHC injection alone. Additional results from the swine model at a large injection volume showed a higher level of pro-angiogenic response with mfNHC-MS-C delivery compared to the mfNHC injection. These results highlighted the potential of the injectable mfNHC as a cell delivery matrix by augmenting host cell infiltration and pro-angiogenesis response.

4. Experimental Section

Materials:

Sodium hyaluronate with molecular weight of 1.5×10^6 Da (HA, research grade) was purchased from LifeCore Biomedical Inc. (Chaska, MN, USA). Glycidyl acrylate (GA) was obtained from TCI America Inc. (Portland, OR, USA). The poly (ethylene glycol) dithiol (HS-PEG-SH) with an average MW of 5 kDa (PEG-SH, MW 5 kDa) was from JenKem Technology (Plano, TX, USA). All other chemical reagents were purchased from Sigma-Aldrich (St. Louis, MO, USA) unless otherwise noted.

Acrylate Modification of Sodium Hyaluronate and mfNHC Fabrication:

Glycidyl acrylate (GA) was added to an HA solution in phosphate buffer saline (PBS) (pH 8.5, 1 w/w%) at a volume ratio of 3:100. The mixture was gently mixed with a magnetic stirrer at 37 °C for 16 h and then precipitated into ethanol at a 10-fold volume of the solution. The obtained acrylated HA (HA-Ac) was washed with ethanol and air-dried. The acylation degree was determined by the Ellman's assay. The functionalized electrospun PCL nanofiber fragments with an average length of 50 μm were produced according to a protocol that we reported previously.^[16, 17] Briefly, PCL nanofibers were electrospun by extruding a PCL solution (16 w/w%, in 9:1 (v/v) dichloromethane and dimethylformamide) from a 5-mL syringe through a metallic 27-G needle at a rate of 2.5 mL h⁻¹ with an electric potential of 16 kV between the grounded collector (a plate at a 900-rpm rotation rate) and the needle. To label PCL fibres, a polymer fluorescent dye, poly (9, 9-dioctylfluorene-alt-benzothiadiazole) (F8BT) was added to the PCL solution. The dried PCL fibres were plasma treated to generate carboxylic groups, which were activated and converted these functional groups to maleimide (MAL) groups by treating the fibres with ethyl dimethylaminopropyl carbodiimide (EDC) and N-hydroxysuccinimide (NHS) at a molar ratio of 1:4:4 for carboxyl groups:EDC:NHS and then reacting with N-(2-aminoethyl)

maleimide (AE-MAL) at a molar ratio of carboxyl groups to AE-MAL of 1:2 at room temperature for 12 h. The MAL-modified PCL fibres were fragmented using a cryogenic mill (Freezer/Mill 6770, SPEX SamplePrep, Metuchen, NJ), washed, lyophilized, and stored at $-20\text{ }^{\circ}\text{C}$ before use.

The NHC was prepared by mixing 30 mg mL^{-1} of MAL-fibre fragments in 10 mg mL^{-1} of HA-Ac solution in PBS (pH 7.4) with 5 mg mL^{-1} of PEGSH in water. Crosslinking between HA-Ac and PEG-SH and between MAL-fibres and PEG-SH was mediated by a Michael addition reaction, which occurs at $37\text{ }^{\circ}\text{C}$ without any additives or by-products. The NHC was then mechanically fragmented by passing it through a stainless-steel mesh with a nominal pore opening of 0.003, 0.006, or 0.009 inches to generate mfNHC with different sizes. As shown in Figure 1A, the pre-formed NHC was loaded in two syringes connected with a union fitted with a stainless-steel mesh with defined pore opening. The NHC was pushed through the mesh back and forth twice. The mfNHC generated with this simple method consists of microgels with aspherical shape and a relatively narrow size distribution. The average size of the mfNHC can be controlled by the mesh size of the screen used in the mechanical fragmentation process.

Mechanical Properties Assessment of the mfNHC:

The storage modulus of the NHC was measured using an ARG2 rheometer (ARG2, TA Instruments) was used to measure the shear storage modulus G' . The mfNHC was injected onto the sample holder and trimmed into an 8-mm disc to fit the dimensions of the parallel plates. A sweep amplitude mode (0.01–10% strain) was used to find the linear amplitude range for each sample. An amplitude within the linear range was chosen to run a frequency sweep (0.1 – 10 Hz). At least three samples were measured for each condition. The injection force of NHC bulk gel and mfNHC were assessed by extruding a 500- μL sample through a 27-G, 13-mm length NIPRO needle attached to a 1-mL syringe on an Instron 34SC-05 load frame (Norwood, MA). The data were presented as the average injection force for three replicates.

IACUC Approval for Animal Experiments:

All protocols for injection and surgical procedures in rat and swine models as well as animal care measures were approved by the Institutional Animal Care and Use Committee at the Johns Hopkins School of Medicine according to guidelines established by the National Institutes of Health and American Association for the Accreditation of Laboratory Animal Care.

Subcutaneous Injection of mfNHC in Rats:

To investigate composite-mediated angiogenesis *in vivo*, composites and hydrogels were injected into the subcutaneous dorsum of 6–8 weeks old Sprague Dawley (SD) rats (both male and female rats were used). Each rat received 6 injections (200 μL per injection) at randomly assigned locations. Rats were sacrificed at predetermined times after injection (post-operative days, POD 7, 14, and 28). Explants reserved for immunohistochemistry were immediately placed within tubes containing 4 w/v% paraformaldehyde.

Explanted Cell Survival In Vivo:

SD rat bone marrow-derived mesenchymal stem cells (RASM-X-01101, Cyagen Biosciences) were maintained and expanded in rat MSC growth medium (GUXMX-90011, Cyagen Biosciences) according to the manufacturer's instructions. MSCs between passages 4 and 6 were used. SD rats were anesthetized using continuous application of aerosolized isoflurane (3 v/v%) during the procedure.

To evaluate the effectiveness of mfNHC for MSC delivery *in vivo*, MSCs were stained with DiR (1,1'-dioctadecyl-3,3,3',3'-tetramethylindotricarbocyanine iodide) to monitor local cell retention at the injection site. Stained cells (one million) were either mixed with 200 μ L of mfNHC or the NHC precursor and injected subcutaneously (s.c.). As a control, one million MSCs in 200 μ L of PBS were injected using the same method. Cell retention at the injection site was monitored for 2 weeks with an *in vivo* Imaging System (IVIS, Perkin Elmer IVIS Lumina II); and relative cell retention was quantified in reference to the bioluminescent signal intensity on Day 0. For each image acquisition, a grey scale body surface image was collected, followed by an overlay of the fluorescent (Ex: 750 nm, Em: 782 nm) and their radiant efficiency were quantified using a live imaging software (Caliper LifeSciences).

Magnetic Resonance Imaging (MRI) Scanning:

A Bruker Biospec 11.7-T MRI system (Bruker, Billerica, MA) was used to image the injected grafts in the axial orientation. Briefly, the animals were immobilized gently in the slice encoding direction and the MRI protocol utilized a T2-weighted axial turbo spin echo pulse sequence with fat suppression. The imaging parameters used were as follows: repetition time at 4000 ms, echo time at 20 ms, echo spacing of 6.7 ms, excitation angle at 85°, refocusing angle at 68°, reference power at 80 W, receiver gain at 101, reference and working frequencies at 500 MHz, and bandwidth at 100 kHz. The images were captured at an acquisition and encoding duration of 3.5 ms and 0.3 ms, respectively, and the image size was 320 \times 320 pixels which represented a field of view of 55 \times 55 mm. Each MRI scan consisted of 51 slices with 1-mm thick each and was completed within about 6 min. The acquired images were processed and analysed using ImageJ (NIH, Bethesda, MD). The volume of each individual graft was traced over a time course of 28 days and volume retention was calculated by normalizing the volume of a graft at a designated time point in reference to its corresponding value on Day 0.

Histological Assessment:

Fixed samples were dehydrated in a graded ethanol series (70% – 100%), embedded in paraffin, and then sectioned. Hematoxylin & eosin staining (H&E) and Masson's trichrome (MAS) staining were performed on 4- μ m tissue sections according to the standard procedures. An image analysis system (Image J, NIH) was used to outline the host cell infiltrated area inside the implant, and to calculate the percentage of cell infiltration area to the whole section area of the implant. Quantitative analysis was conducted by team members in a blinded manner.

Cells Isolation and Flow Cytometry Analysis:

Flow cytometry was applied to identify and quantify the types of cells infiltrated into the matrix and remodelling site. Briefly, the implants were dissected, and surrounding tissue was removed with care. Dissociated explants were digested using hyaluronidase (7 mg mL⁻¹, H3506, Sigma-Aldrich) at 37 °C for 30 min. Tissue suspension were then pushed through 70-µm strainers; and cells were collected by centrifuge at 300 ×g for 5 min. The supernatant was decanted, and the pellet was resuspended with an ice-cold FACS buffer prepared with Ca²⁺/Mg²⁺ free PBS, 1% BSA, 5 mM EDTA and 1% sodium azide. The cell pellet was washed with staining buffer 3 times and stained with specific antibodies in a total volume of 100 µL for 20 min in the dark at 4 °C. The stained cells were washed twice with 1 mL of PBS, then resuspended in 500 µL PBS for flow cytometry analysis. The antibodies used were Alexa Flour 647 anti-rat CD68/SR-D1 (Novus Biologicals), PE/Cy5.5 anti-rat CD163 (Novus Biologicals), PE anti-rat CD38 (BioLegend). Flow data was acquired on SH800 (Sony Biotechnology) and analysed using the FlowJo software.

Immunofluorescence Staining:

To determine the infiltrated cell type inside the mfNHC construct *in-vivo*, the following groups: mfNHC alone, mfNHC-MSC, and MSC suspension, were included. Different materials were injected subcutaneously on the dorsal side of the SD rats. Animals were sacrificed at predefined time point and the injections were retrieved, sectioned for immunofluorescent staining at POD 3, 14 and 28. The fixed collected tissues were sectioned and permeabilized with 0.5% Triton X-100 in PBS, immune-blocked with 4% donkey serum for 2 h, and then incubated with primary antibodies (Table S1 in supporting information) overnight at 4 °C. After washing three times with PBS, tissue sections were incubated for 2 h with Cy5-or Cy3-conjugated secondary antibodies (Table S2 in supporting information), washed three times with PBS, counterstained for 10 min at room temperature with the nuclear stain, DAPI (4',6-diamidino-2-phenylindole dihydrochloride, 2 µg mL⁻¹; Thermo Fisher), and mounted with glass slips in anti-fade fluorescent mounting medium (Dako). Sections were stored at 4 °C until analysis under a Zeiss LSM 510 Meta Confocal Microscope.

Proteome Profiler Array Analysis:

To characterize the inflammation- and regeneration-related cytokines and chemokines mediated by the injected mfNHC and/or MSCs, a rat cytokine antibody proteome profiler array (ARY030, R&D Systems) was used to analyse the tissue samples collected at POD 14 and 28. Each tissue sample was washed with sterile PBS and mixed with a protease inhibitor cocktail (Promega, Madison, WI). The tissue was then cut into pieces followed with homogenization. Arrays were applied on the control group (the normal tissue), the mfNHC group, and mfNHC-MSC group following the manufacturer's protocol. The relative levels of cytokines were quantified using ImageJ software.

Assessment of mfNHC in a Swine Model:

Primary MSCs were isolated from pig adipose tissue and cultured as reported.^[25] For *in-vivo* experiments, allogeneic source of MSCs between passages 4 and 6 were used;

mfNHC or the mfNHC-MSK was injected into the subcutaneous abdomen of swine. Animals were sacrificed at predefined time point and the injections were retrieved, sectioned for immunofluorescent staining at POD 14 and 56. Volume retention of the implants were estimated by using a calliper to measure the height and width. Cell infiltration and endothelial cell density inside the implants were tested under the same approaches as the rat model.

Statistical Analysis:

All values are depicted as *Mean ± Standard Error of the Mean* unless stated otherwise. Statistical comparisons were performed using GraphPad Prism 8.0. The significance between two groups was analysed using a two-tailed Student *t*-test. The significance between multiple groups was analysed by a one-way ANOVA. A difference was considered statistically significant when $P < 0.05$.

Supplementary Material

Refer to Web version on PubMed Central for supplementary material.

Acknowledgements

This work was supported by a research contract from LifeSprout Inc. (HQM and SKR), the Maryland Stem Cell Research Fund (No. MSCRFL5375, SKR and HQM), the Helmsley Foundation (FMS and HQM), and the National Institutes of Health (NIDCR R01DE031488, SKR, HQM, and YHY).

References

1. Van Belleghem S; Torres L Jr; Santoro M; Mahadik B; Wolfand A; Kofinas P; Fisher JP, *Advanced functional materials* 2020, 30 (3), 1907145.
2. Wang C; Poon S; Murali S; Koo C-Y; Bell TJ; Hinkley SF; Yeong H; Bhakoo K; Nurcombe V; Cool SM, *Biomaterials* 2014, 35 (25), 6776–6786. [PubMed: 24854095]
3. Ruehle M; Eastburn E; LaBelle S; Krishnan L; Weiss J; Boerckel J; Wood L; Guldborg R; Willett N, *Science advances* 2020, 6 (34), eabb6351.
4. Chang C; Yan J; Yao Z; Zhang C; Li X; Mao HQ, *Advanced healthcare materials* 2021, 10 (7), 2001689.
5. Xu R; Zhang F; Chai R; Zhou W; Hu M; Liu B; Chen X; Liu M; Xu Q; Liu N, *Journal of cellular and molecular medicine* 2019, 23 (11), 7617–7631. [PubMed: 31557396]
6. Laflamme MA; Chen KY; Naumova AV; Muskheli V; Fugate JA; Dupras SK; Reinecke H; Xu C; Hassanipour M; Police S, *Nature biotechnology* 2007, 25 (9), 1015–1024.
7. Caplan H; Olson SD; Kumar A; George M; Prabhakara KS; Wenzel P; Bedi S; Toledano-Furman NE; Triolo F; Kamhieh-Milz J, *Frontiers in immunology* 2019, 10, 1645. [PubMed: 31417542]
8. Moll G; Ankrum JA; Kamhieh-Milz J; Bieback K; Ringdén O; Volk H-D; Geissler S; Reinke P, *Trends in molecular medicine* 2019, 25 (2), 149–163. [PubMed: 30711482]
9. Drzeniek NM; Mazzocchi A; Schlickeiser S; Forsythe SD; Moll G; Geißler S; Reinke P; Gossen M; Gorantla VS; Volk H-D, *Biofabrication* 2021, 13 (4), 045002.
10. Koh J; Griffin DR; Archang MM; Feng AC; Horn T; Margolis M; Zalazar D; Segura T; Scumpia PO; Di Carlo D, *Small* 2019, 15 (39), 1903147.
11. Barati D; Watkins K; Wang Z; Yang F, *Small* 2020, 16 (22), 1905820.
12. Tong X; Yang F, *Advanced healthcare materials* 2018, 7 (7), 1701065.
13. Bidarra SJ; Barrias CC; Granja PL, *Acta biomaterialia* 2014, 10 (4), 1646–1662. [PubMed: 24334143]

14. Lam J; Lowry WE; Carmichael ST; Segura T, *Advanced functional materials* 2014, 24 (44), 7053–7062. [PubMed: 26213530]
15. Knopf-Marques H; Pravda M; Wolfova L; Velebny V; Schaaf P; Vrana NE; Lavalle P, *Advanced healthcare materials* 2016, 5 (22), 2841–2855. [PubMed: 27709832]
16. Li X; Cho B; Martin R; Seu M; Zhang C; Zhou Z; Choi JS; Jiang X; Chen L; Walia G, *Science translational medicine* 2019, 11 (490).
17. Li X; Zhang C; Haggerty AE; Yan J; Lan M; Seu M; Yang M; Marlow MM; Maldonado-Lasunción I; Cho B, *Biomaterials* 2020, 245, 119978.
18. Aguado BA; Mulyasmita W; Su J; Lampe KJ; Heilshorn SC, *Tissue Engineering Part A* 2012, 18 (7–8), 806–815. [PubMed: 22011213]
19. Zhang Z; Gupte MJ; Jin X; Ma PX, *Advanced functional materials* 2015, 25 (3), 350–360. [PubMed: 26069467]
20. Rao N; Agmon G; Tierney MT; Ungerleider JL; Braden RL; Sacco A; Christman KL, *ACS nano* 2017, 11 (4), 3851–3859. [PubMed: 28323411]
21. Feng Q; Li Q; Wen H; Chen J; Liang M; Huang H; Lan D; Dong H; Cao X, *Advanced Functional Materials* 2019, 29 (50), 1906690.
22. Muir VG; Qazi TH; Shan J; Groll J.r.; Burdick JA, *ACS Biomaterials Science & Engineering* 2021, 7 (9), 4269–4281. [PubMed: 33591726]
23. Chang S; Finklea F; Williams B; Hammons H; Hodge A; Scott S; Lipke E, *Biotechnology Progress* 2020, 36 (4), e2986.
24. Daly AC; Riley L; Segura T; Burdick JA, *Nature Reviews Materials* 2020, 5 (1), 20–43.
25. Chen Y-J; Liu H-Y; Chang Y-T; Cheng Y-H; Mersmann HJ; Kuo W-H; Ding S-T, *JoVE (Journal of Visualized Experiments)* 2016, (109), e53886.
26. Agarwal N; Varma IK; Choudhary V, *Journal of applied polymer science* 2006, 99 (5), 2414–2420.
27. Xiao L; Tong Z; Chen Y; Pochan DJ; Sabanayagam CR; Jia X, *Biomacromolecules* 2013, 14 (11), 3808–3819. [PubMed: 24093583]
28. Qu J; Zhao X; Liang Y; Zhang T; Ma PX; Guo B, *Biomaterials* 2018, 183, 185–199. [PubMed: 30172244]
29. Bian L; Hou C; Tous E; Rai R; Mauck RL; Burdick JA, *Biomaterials* 2013, 34 (2), 413–421. [PubMed: 23084553]
30. Liu S; Guo W, *Advanced Functional Materials* 2018, 28 (41), 1800596.
31. Shazeeb MS; Corazzini R; Konowicz PA; Fogle R; Bangari DS; Johnson J; Ying X; Dhal PK, *Biomaterials* 2018, 178, 326–338. [PubMed: 29861090]
32. Bund T; Nikitina E; Chakraborty D; Ernst C; Gunst K; Boneva B; Tessmer C; Volk N; Brobeil A; Weber A, *Proceedings of the National Academy of Sciences* 2021, 118 (12).
33. Amici SA; Young NA; Narvaez-Miranda J; Jablonski KA; Arcos J; Rosas L; Papenfuss TL; Torrelles JB; Jarjour WN; Guerau-de-Arellano M, *Frontiers in immunology* 2018, 9, 1593. [PubMed: 30042766]
34. Alvarado-Vazquez PA; Bernal L; Paige CA; Grosick RL; Vilriales CM; Ferreira DW; Ulecia-Morón C; Romero-Sandoval EA, *Immunobiology* 2017, 222 (8–9), 900–912. [PubMed: 28545809]
35. Lee CZ; Kozaki T; Ginhoux F, *Nature Reviews Immunology* 2018, 18 (11), 716–725.
36. Yang C; Zhao C; Wang X; Shi M; Zhu Y; Jing L; Wu C; Chang J, *Nanoscale* 2019, 11 (38), 17699–17708.
37. Wang Y; Li C; Wan Y; Qi M; Chen Q; Sun Y; Sun X; Fang J; Fu L; Xu L, *Small* 2021, 17 (41), 2101505.
38. Kang H; Yang B; Zhang K; Pan Q; Yuan W; Li G; Bian L, *Nature communications* 2019, 10 (1), 1–14.
39. Wang M; Yuan Q; Xie L, *Stem cells international* 2018, 2018.
40. Seo Y; Kim H-S; Hong I-S, *Stem cells international* 2019, 2019.
41. Kouroupis D; Sanjurjo-Rodriguez C; Jones E; Correa D, *Tissue Engineering Part B: Reviews* 2019, 25 (1), 55–77.

42. Kot M; Musiał-Wysocka A; Lasota M; Ulman A; Majka M, Acta Biochimica Polonica 2019, 66 (4), 499–507. [PubMed: 31883363]

Author Manuscript

Author Manuscript

Author Manuscript

Author Manuscript

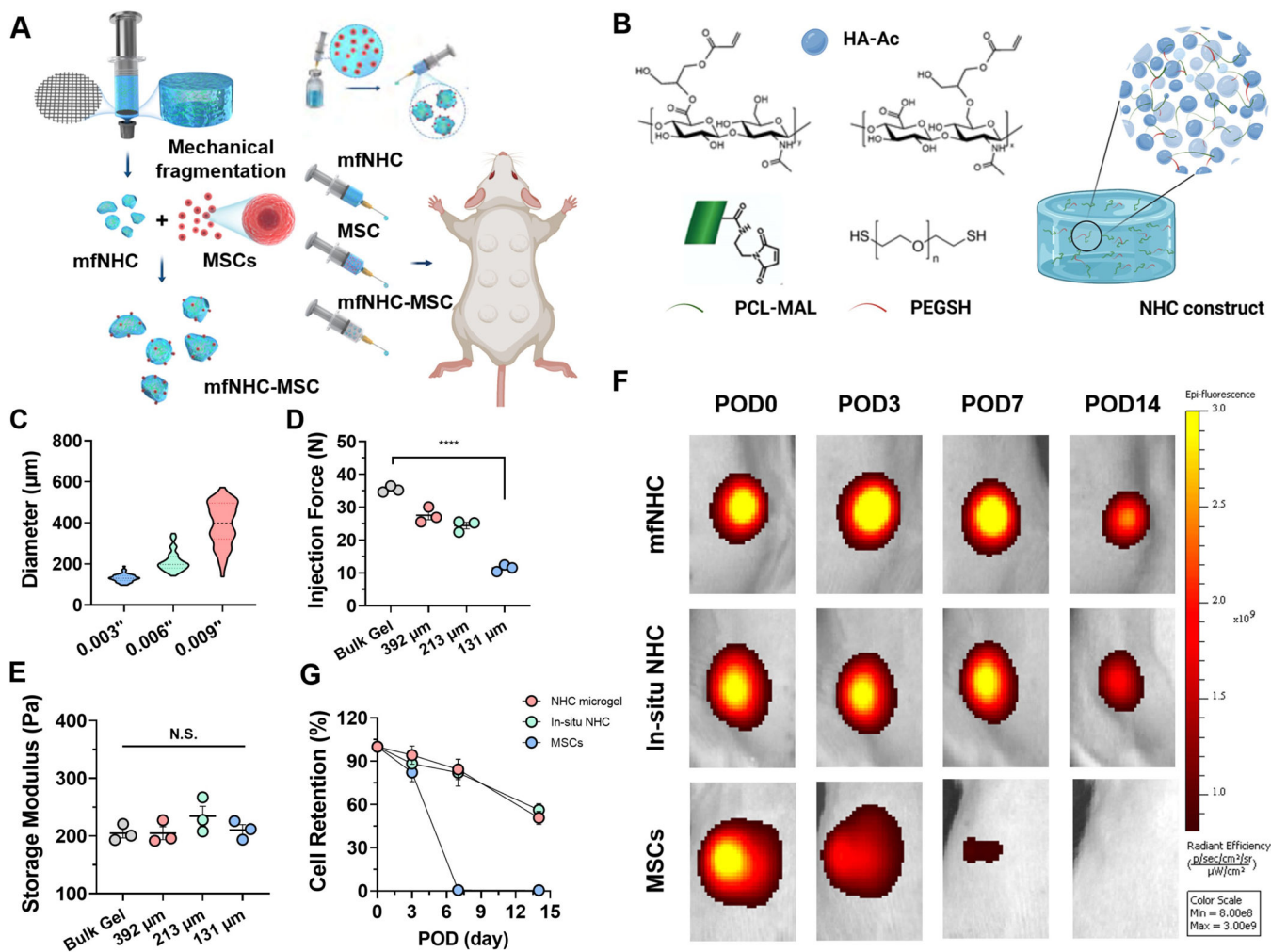


Figure 1. Synthesis and characterization of mfNHC and retention of subcutaneously delivered MSCs delivered with mfNHC in SD rats.

(A) Engineered mfNHC were mechanically fragmented by pushing the bulk gel through mesh screens with different sizes of pore openings, *in-vivo* soft tissue remodelling process was evaluated by subcutaneously injecting the mfNHC, MSC and NHC-MSC on the dorsal side of rats. (B) Schematic of structure and synthesis of NHC. (C) Size distribution of mfNHC prepared with different mesh sizes (n = 100). (D) Decreased injection force of mfNHC with reducing diameter. (E) Effect of mfNHC size on shear storage modulus G' (n = 3). (F) Representative IVIS images of DiR-labeled MSCs following subcutaneously injection in SD rats when delivered with either NHC bulk gel or mfNHC (131 μm) on PODs 0, 3, 7, and 14 (n = 3). (G) Relative cell retention at different time points in reference to the signals collected right after injection on day 0 (n = 3). The significance between two groups was analysed using two-tailed Student t-test. The significance between multiple groups was analysed by a one-way ANOVA. *N.S.* $P > 0.05$, ****** $P < 0.0001$. Data are presented as *Mean ± Standard Error of the Mean*.

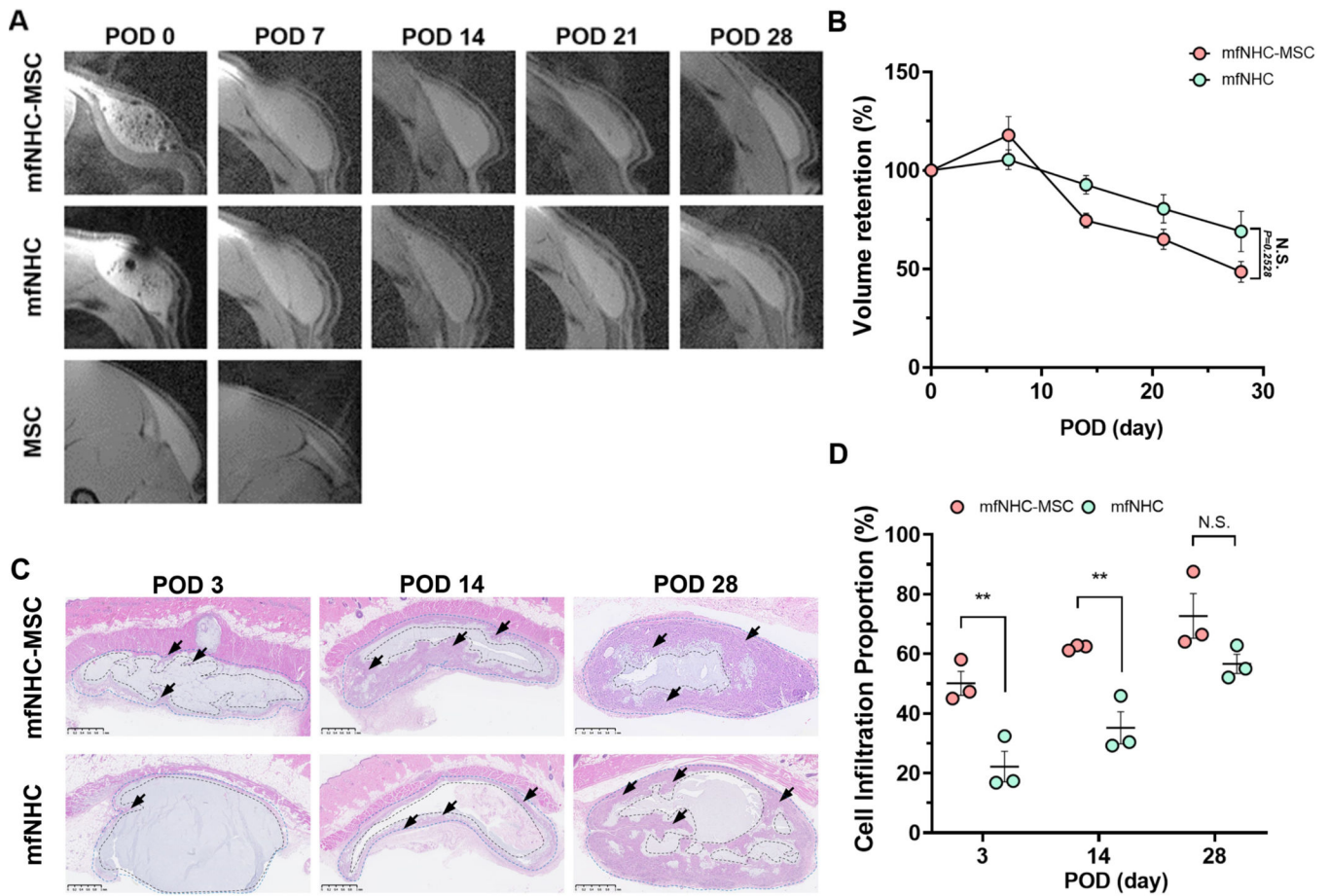


Figure 2. The retention of and cell infiltration into the subcutaneously injected mfNHC with (mfNHC-MSC group) or without MSCs (mfNHC group) over 28 days following injection in SD rats.

(A) Representative images of the injected matrix and/or MSCs every 7 days after injection.

(B) Quantitative analysis of relative volume retention after injection (n = 6). (C) H&E staining showing cell infiltration in the mfNHC with (mfNHC-MSC group) or without MSCs (mfNHC group) at POD 3, 14, and 28. The arrows indicate host cell infiltrated boundary. Scale bar: 1 mm.

(D) Quantitative analysis showing the relative percentage host cell infiltration area inside the matrix over 28 days (n = 3). Statistical significance was calculated by two-tailed Student t-test. ^{N.S.}P>0.05, ^{**}P<0.01. Data are presented as *Mean ± Standard Error of the Mean*.

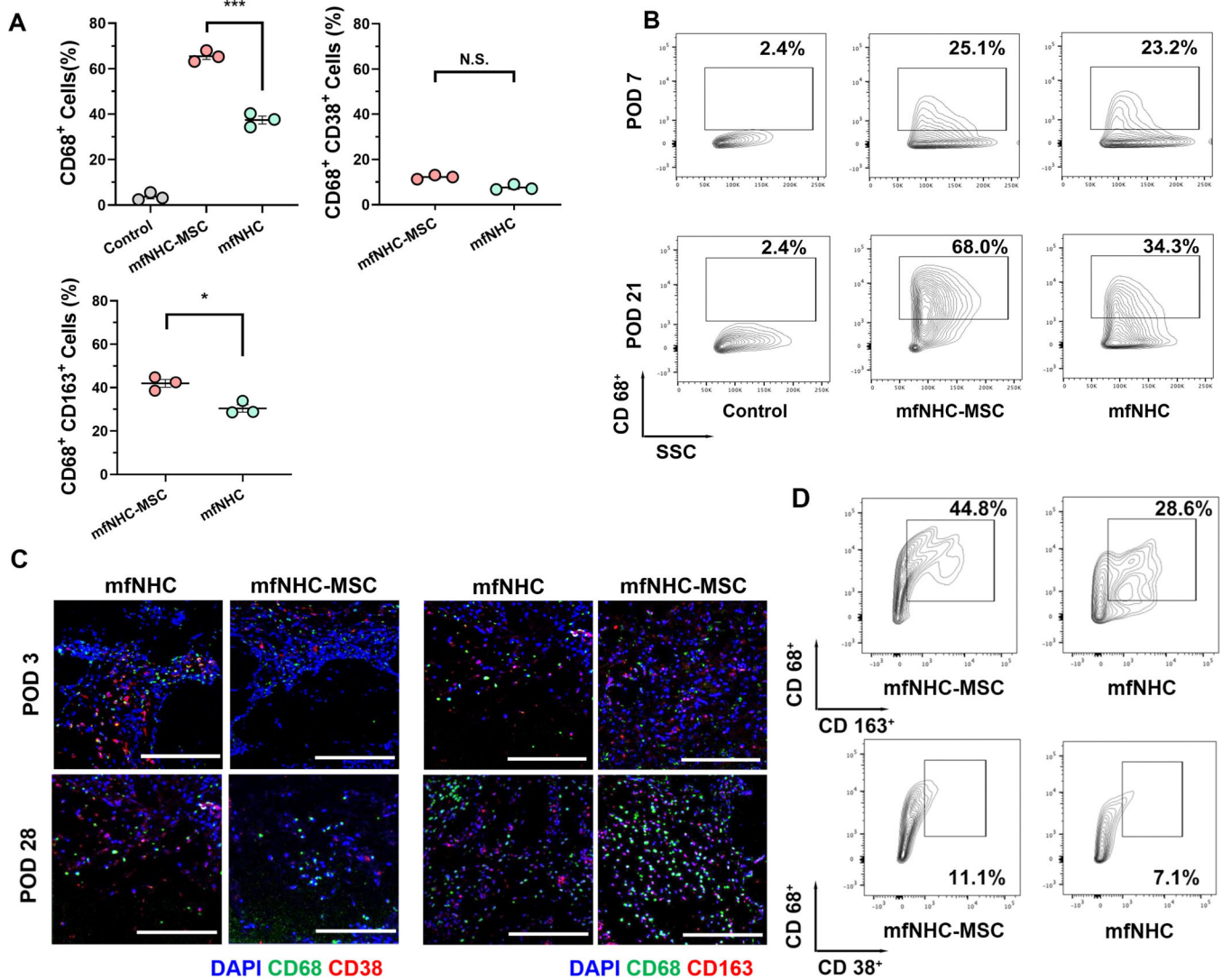


Figure 3. Infiltration of monocytes and macrophages and their phenotypes in the subcutaneously injected mfNHC with/without MSCs.

(A) CD68⁺ cells, CD68⁺CD163⁺ cells and CD68⁺CD38⁺ cell proportion inside the implants at POD 21 in SD rats (n = 3). (B) Representative FACS data of infiltrated CD68⁺ cells showing the macrophages recruitment at PODs 7 and 21. (C) Macrophages infiltrated into mfNHC and mfNHC-MSC at POD 3 and 28. CD38⁺ and CD163⁺ cells (shown in green) were found in penetrated from the boundary to the implant interior over time. Scale bar: 200 μ m. (D) Quantitative data showing proportion of CD163⁺ (M2-like macrophages) and CD38⁺ (M1-like macrophages) cells gated on CD68⁺ at POD 21. The significance between two groups was analysed using two-tailed Student t-test. The significance between multiple groups was analysed by a one-way ANOVA. N.S.: $P > 0.05$, * $P < 0.05$, ** $P < 0.01$, *** $P < 0.001$. Data are presented as *Mean \pm Standard Error of the Mean*.

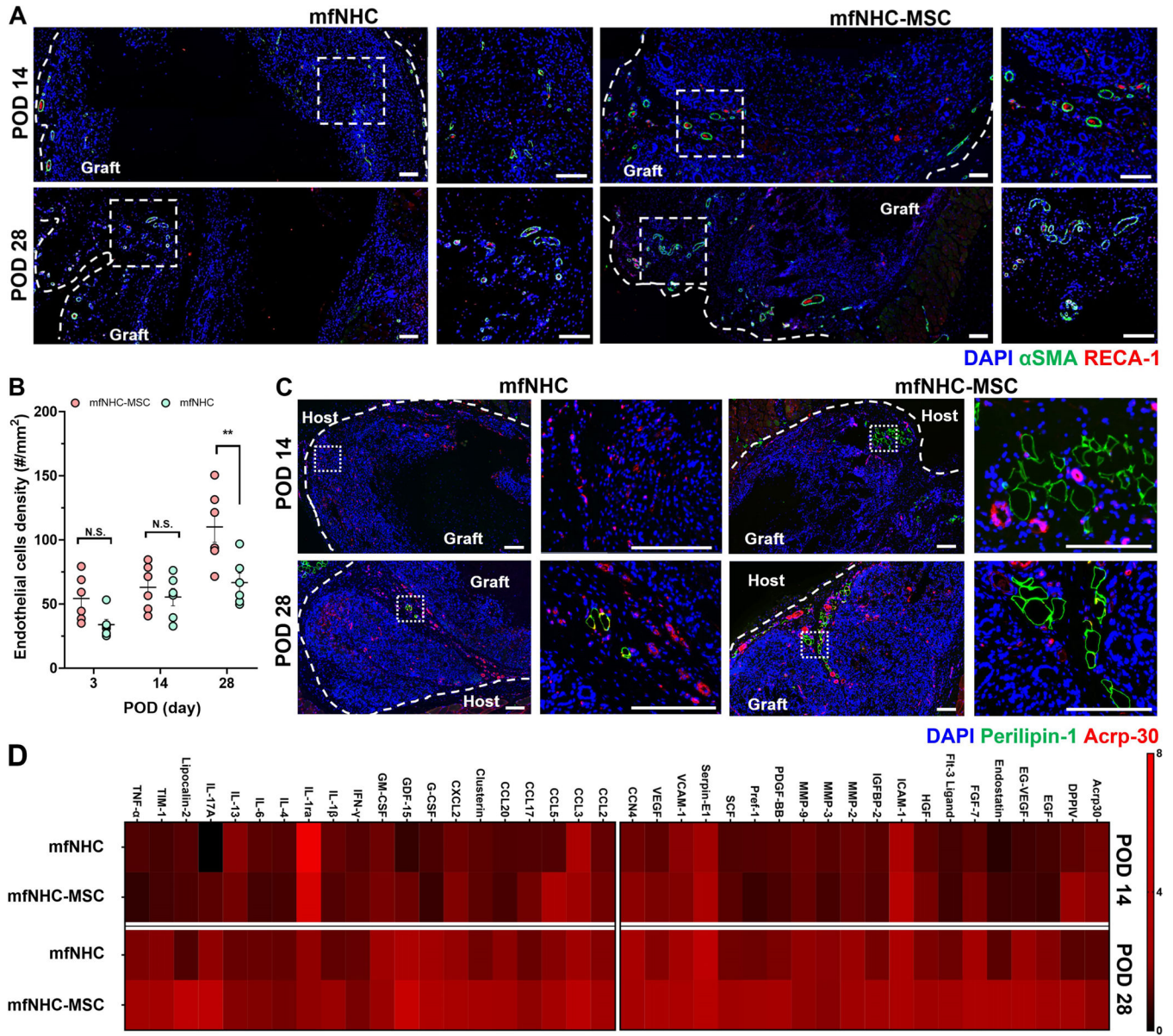


Figure 4. Angiogenesis and tissue remodelling process in mfNHC with (mfNHC-MSC group) or without MSCs (mfNHC group) in SD rats.

(A) Representative immunofluorescent staining images showing the infiltrated endothelial cells (stained with RECA-1 in red and alpha smooth muscle actin, α SMA, in green) inside the matrices at POD 14 and 28. Scale bar: 100 μ m. (B) Quantitative data presenting the infiltrated endothelial cells density in the matrix over 28 days (n = 6). (C) Immunofluorescent staining images showing the adipogenesis inside the matrix at POD 14 and 28; perilipin-1 was stained in green, and adiponectin-1 stained with Acrp-30 in red. Scale bar: 200 μ m. (D) Profiling of immunomodulation (left) and tissue remodelling (right) cytokine proteins production in mfNHC and mfNHC-MSC matrix at POD 14 and 28. Statistical significance was calculated by two-tailed Student t-test. N.S. P>0.05, **P<0.01. Data are presented as *Mean \pm Standard Error of the Mean*.

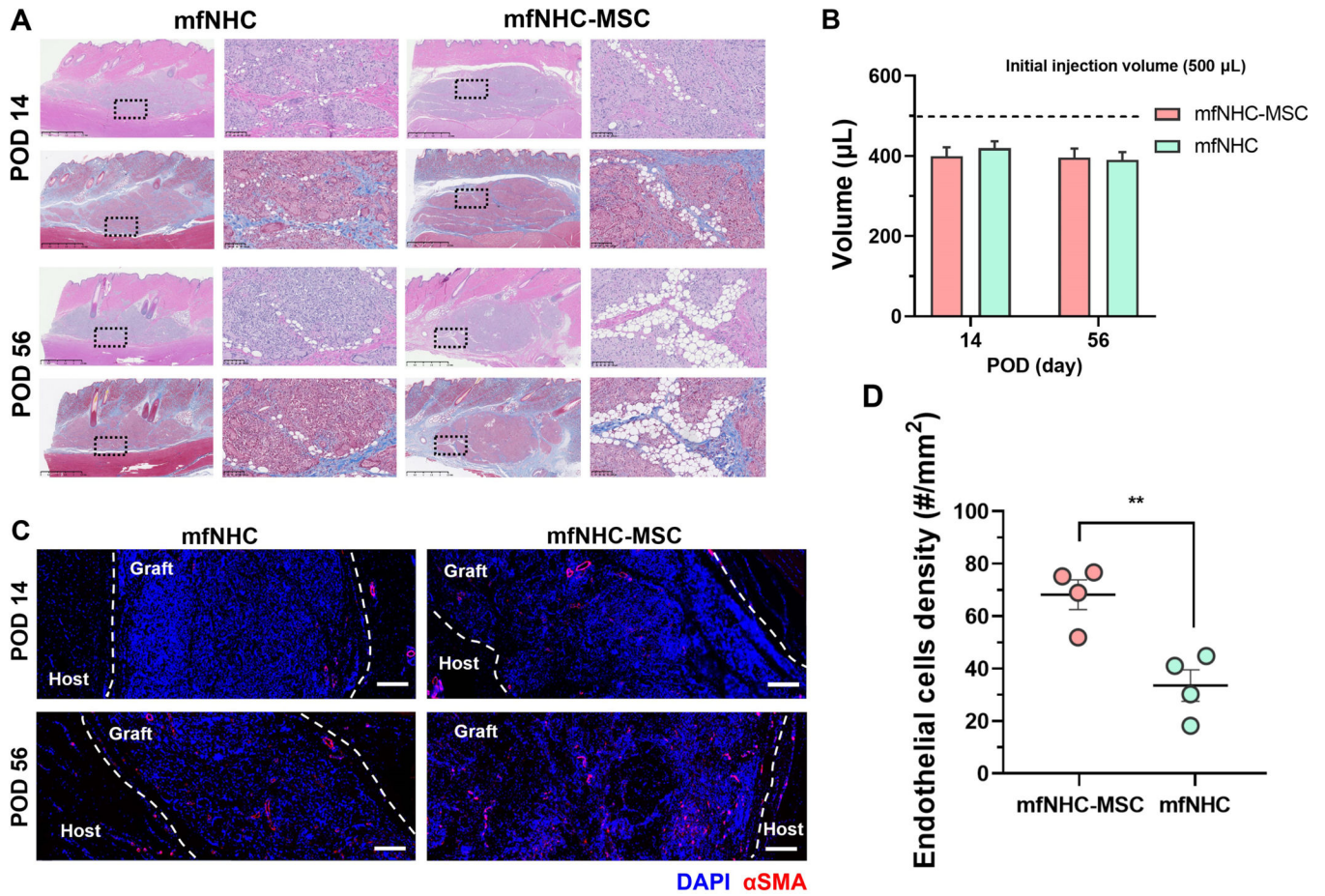


Figure 5. Host cell infiltration and tissue remodelling mediated by mfNHC with or without MSCs in a swine model.

(A) H&E and Masson's trichrome staining showing cell infiltration in the injected matrix. Scale bar for the broad view images: 2.5 mm, Scale bar for the zoom-in images: 100 μ m. (B) Volume retention of the constructs over 56 days after injection (n = 4). (C) Immunofluorescent staining images showing the infiltrated endothelial cells (stained for α SMA in red) inside the constructs at POD 14 and 56. Scale bar: 200 μ m. (D) The density of infiltrated endothelial cells in the construct at POD 14 (n = 4). Statistical significance was calculated by two-tailed Student t-test. ^{N.S.}P>0.05, ^{**}P<0.01. Data are presented as *Mean \pm Standard Error of the Mean*.